Microelectronics Reliability 52 (2012) 361–374

Contents lists available at SciVerse ScienceDirect

Microelectronics Reliability

journal homepage: www.elsevier.com/locate/microrel

Invited Paper

Low temperature nanointegration for emerging biomedical applications

Matiar M. R. Howlader *, Thomas E. Doyle

Department of Electrical and Computer Engineering, McMaster University, 1280 Main Street West, Hamilton, Canada L8S 4K1

ARTICLE INFO

Article history:
Received 15 May 2011
Received in revised form 22 August 2011
Accepted 25 August 2011
Available online 23 September 2011

ABSTRACT

In this paper, surface activated nanointegration of computational, electrical, optical, and mechanical structures for intelligent telemetry, communication, and sensing systems is described. The design approach and integration of top-down systems and bottom-up devices is considered with the need for biologically compatible bonding. For the simplified interface between bottom-up and top-down design a bus-bar unit architecture is presented. Emerging biomedical applications using intelligent sensors for remote patient monitoring and systems for rehabilitation comparing surface vs. implanted sensors are considered. Requirements for nanointegration of biomedical systems are suggested. Diverse combinations of rigid and flexible substrates of copper, gold, gallium arsenide, gallium phosphide and liquid crystal polymer were bonded by using two different nanobonding techniques. In these techniques, the surface cleaning with/without simultaneous deposition of nano-adhesion layers and contact in ultra-high vacuum/high vacuum were accomplished. These nanobonding technologies provide void-free, strong, and nanometer scale covalent bonding at room temperature or at low temperatures (~240 °C), and do not require chemicals, adhesives, or high external pressure. A considerable electrical current conduction and low loss of the nanobonded laminate was observed at high frequency. This investigation reveals that a biocompatible, high performance, and miniaturized systems may be realized for intelligent, implantable biomedical sensors because of the strong bond, low toxicity and favorable electrical properties in surface activated nanobonding.

1. Introduction

Nanointegration is the integration of computational, electrical, optical, and fluidic structures at nanometer scale for low-cost intelligent modules that provide telemetry, communication, and control of target systems. Perhaps the most important area of nanointegration impact will be in biomedical systems [1–3]. Aging populations and increasing needs for remote healthcare monitoring will require intelligent non-invasive sensors for physiological data logging for clinical decision support systems. The care and rehabilitation of this increasing population will also require systems to aid in embedded real-time drug delivery and systems [4,5] for the rehabilitation or restoration of decreased physical ability.

With clear impetus for such systems, this paper seeks to address a framework of how such systems may be realized with present technology and design methodology. Pure top-down, or bottom-up design methodology presents some challenges when the single approach is done without consideration of the technology (top-down) [6–8] or without consideration of the system (bottom-up) [9,10]. The authors believe this challenge is primarily born of the complexities of the respective design problem and the skill set of the designer(s) (i.e., system designers vs. nanodevice designers). Fig. 1 illustrates an intersection of the top-down engineering/system design approach with the bottom-up nanostructure design approach. Nanointegration through simplified interface between bottom-up and top-down using a bus-bar unit architecture can this objective of the goal.

Top-down designs are typically realized using lithographic methods (e.g., electron beam, extreme ultraviolet, nanoimprinting), etching (i.e., focused ion beam), sputtering, and deposition [8,11–13]. While it is clear from Fig. 2 that top-down technology permits the fabrication of sub 100 nm implementation (nano-scale), the associated costs of (re)tooling are unsustainable. In addition, the physical lower limit to silicon is predicted on the verge of its limit [14,15].

Bottom-up design includes template growth and self- and direct assembly processes, for example that creates a structure, such as semiconductor nanowires (NWs), through the manipulation and organization of material and processes at the atomic level [9,10].

The primary challenge presents itself when the two approaches need to be integrated. Prior work detailing the incompatibilities between the speed, size, and cost of integration is well documented in Ref. [16]. The field of nanointegration is necessary to realize the benefit of nano-scale design. Fundamental to the field are the methods of bonding materials for cohesive systems.

* Corresponding author.
E-mail addresses: mrhowlader@ece.mcmaster.ca (M.M.R. Howlader), doylet@mcmaster.ca (T.E. Doyle).

0026-2714/$ - see front matter © 2011 Elsevier Ltd. All rights reserved.
doi:10.1016/j.microrel.2011.08.018

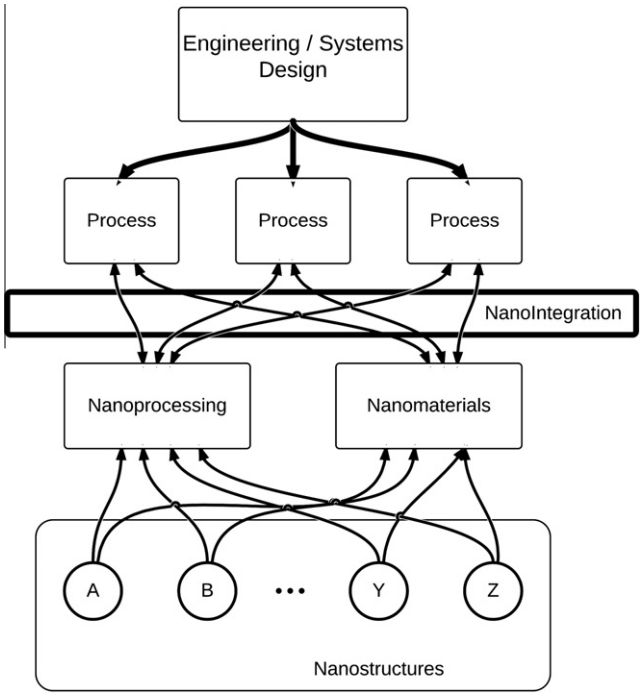

Fig. 1. Illustration of intersection of the top-down engineering/system design approach with the bottom-up nanostructure design approach. Top-down and bottom-up meets through nanointegration.

The present state of nanointegration has several current methods of bonding which are broadly summarized in Table 1 [16–21]. Each bonding method is listed with a primary implementation property. The implementation properties and resultant bonding are imperative factors when biomedical devices are considered.

In this paper, we propose an interconnection architecture for full integration that requires biocompatibility and longevity in application. This interconnection architecture will focus on biomedical integration of external and implantable systems. To this end, we propose that a biocompatible, low-toxicity solution that provides direct adhesion and nano-level bonding.

2. Emerging applications of nanointegration

2.1. Biomedical applications

In this section, we identify emerging applications of nanointegration in biomedical systems. An aging population and a health care system that is opting to treat more patients remotely will require three primary technologies: (1) general health monitoring, (2) acute care monitoring and testing coupled with clinical decision support, and (3) rehabilitative/assistive devices. Fig. 3a illustrates the proposed topology for homogeneous monitoring, care, and education/simulation system. Fig. 3b illustrates the sensor level topology for the Medical Sensor Personal Area Network (MedSPAN). A common implementation requirement of these systems is the wearable, and ultimately implantable, intelligent sensors. These sensors would provide bidirectional communication for physiological telemetry and device control. An intelligent sensor array would not only facilitate care, but also would also allow for the building of better physiological models and support simulation in education and training.

2.1.1. General health monitoring

Supporting the Medical Care and COmmunication Integration (McCOI) system will be a Medical Sensor Personal Area Network

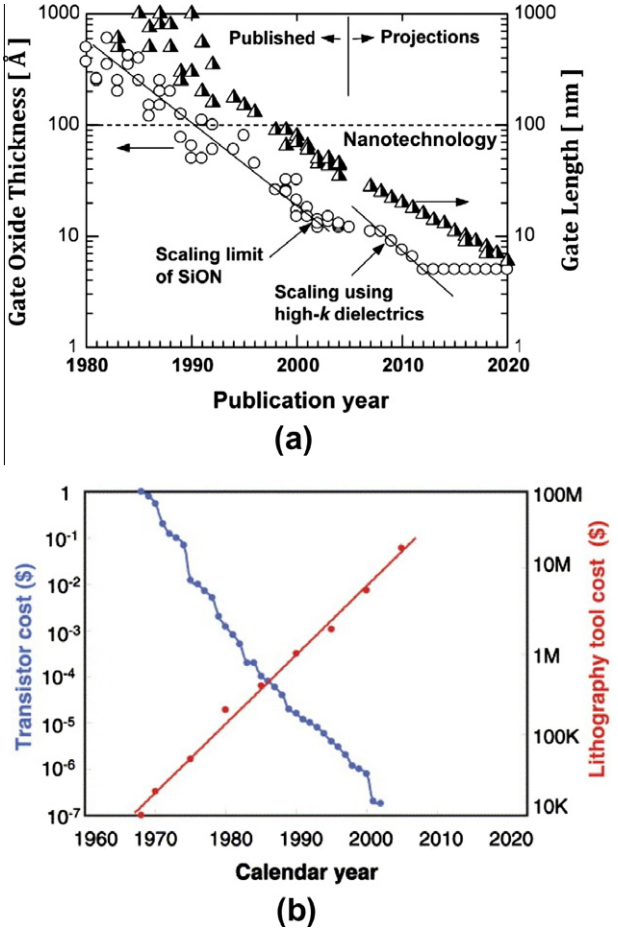

Fig. 2. (a) Nanotechnology with consideration of size lower limit and (b) implementation costs. Scaling trend of gate oxide thickness over the past five technology generations from the 0.18 μm to 65 nm node. Saturation of gate oxide thickness is appeared. Adapted from Refs. [14,15].

Table 1
Bonding methods and implementation properties.

Bonding method	Implementation property
Fusion (hydrophilic and hydrophobic)	High temperature
Thermocompression	High temperature, high external force
Adhesive and chemical	Opaque and chemical sensitivity
Anodic and laser assisted	Size and materials limited
Surface activated (UHV)	Room temperature, high vacuum pressure

(a MedSPAN) that will allow for the monitoring of health vitals. This component will consist of an array of smart, non-invasive, low-power wireless physiological transducers that will transmit measurements to an individual's health monitor processor (typically worn on the body). In general, health-monitoring mode, the array of sensor measurements will be periodically transmitted in bulk to a central McCOI from the processor. The MedSPAN processor will perform sensor array data collection, some basic analysis, trend prediction, and bi-directional communication with the McCOI. If a medical event should occur then the MedSPAN may be reconfigured for targeted vitals and increased data collection and the health monitor processor will convert to Acute Care mode for the real-time streaming of sensor array data.

2.1.2. Acute care

Once in Acute Care mode, McCOI's clinical decision support will provide expert data and support based upon the level severity of

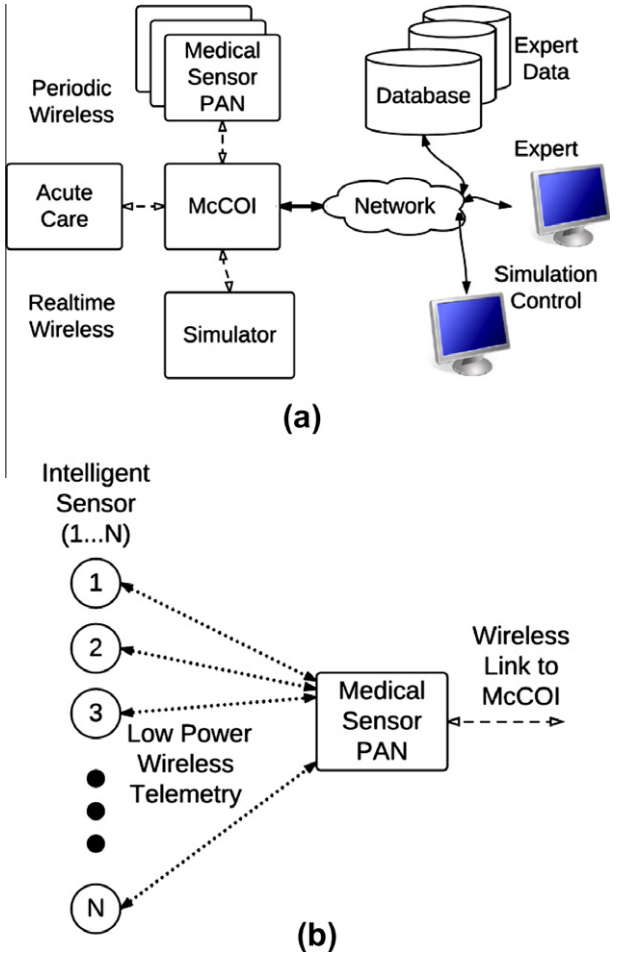

Fig. 3. (a) Topology of a proposed medical care and communication integration (McCOI) platform for patient monitoring, decision support, physiological modeling, and simulation based training using Medical Sensor Personal Area Network (MedSPAN). (b) Overview of the intelligent nano-medical sensor personal area network.

the medical event and recent monitoring of vital data. The Acute Care mode will leverage the MedSPAN infrastructure to transmit real-time sensor array data of the critical vital signs. Based upon the functional level of two-way communication the McCOI will suggest the appropriate clinical decision support system and data management technologies (Expert and Expert Data). The goal of the Acute Care mode is to provide situational awareness and the ability to expedite diagnosis and treatment.

2.1.3. Physiological models, education, and simulation

Expert data and support are crucial for remote acute care; however, teaching and reinforcement of skills are key for medical support personnel. An architecture that supports an integrated approach to general monitoring, acute care, and tele-simulation for education will be the most successful in meeting the care and support needs for both patient and care provider. The architecture should provide a database for individual physiological records that could permit better physiological models based on the aggregate and context. This architecture will support remote acquisition, maintenance, and augmentation of medical personnel knowledge and clinical skills. The Simulation mode would fully integrate with McCOI by leveraging the MedSPAN infrastructure to transmit simulated real-time sensor array data of the critical vital signs.

2.1.4. Rehabilitative and assistive devices

The sensors used for monitoring and acute care decision support are only one application of such bio-sensors. Similar sensors will be employed for prosthetic and/or limb enhancement. Through injury or illness there is great immediate and increasing need for rehabilitative and assistive devices. Individuals that have lost a limb have the option of prosthetic enhancement; however, active (not the traditional passive) and controllable prostheses are becoming possible with methods such as targeted muscle reinnervation and myoelectric pattern recognition [22]. Individuals with weakness, or paralysis, of a limb due to nerve damage are regaining control by systems that bypass the efferent and afferent feedback path with implanted sensors for telemetry and stimulation [22–27].

Examples of modern and emerging rehabilitative and assistive devices:

- Targeted muscle reinnervation at the Rehabilitation Institute of Chicago [22,28] is an emerging method of restoring limb function after amputation. Fig. 4 shows the first recipient of this technology with a schematic of implementation.
- Bionic Neuron (BION) – BION are injectable, single channel microstimulators [25] that provide telemetry and muscle stimulation. These devices assist in control of existing muscles and limbs.
- Brain–Computer-Interfacing (BCI) – BCI is the direct linkage of the brain to a computing device. The degree of invasiveness varies; however, the surface electrodes (non-invasive) methods have shown promise for one- to two-degree control [26,27]. Fig. 5 shows a working BCI system for control of an orthosis and the standard 10–20 placement of electroencephalography (EEG) electrodes.
- Electrocorticography (ECoG) – ECoG is one method of implementing an invasive BCI method where an electrode array is placed directly upon the subject's brain [22,29]. While considered invasive, this is less invasive than using electrode arrays that are inserted into the brain to identify single unit neuron responses. Fig. 6 shows (a) Implanted telemetry and control sensors for a prosthetic hand [32], (b) The Electrocorticographic (ECoG) electrode array overlaid directly on the human brain [33], and (c) Levels of sensor/electrode invasiveness related to BCI [34].

2.2. Intelligent medical sensors

The degree of sensor invasiveness varies from skin surface to brain implant. While surface systems are least invasive, they tend to suffer from lower reliability from unwanted artifacts, long-term stability, increased computational complexity and processing, and typically must be inexpensive enough to be disposable. Implantable systems also have considerable challenges when considering biocompatibility and long-term stability; however, implanted sensors have the advantage, in many cases, because they are at the source of physiological process that provides more reliable data, less data processing, and fixed location.

2.2.1. Wearable intelligent sensors

Non-invasive or minimally invasive intelligent, wireless, and wearable sensors are required to monitor critical vital sign data.

When we consider sensor design for monitoring and acute care, apart from the transducer, these wearable sensors may share a common platform. Fig. 3b illustrates the common platform design overview for a single sensor array for monitoring a subject. Each node measures an electrophysiological property using 1-to-N transducers. The sensor array is composed of 1-to-N nodes. The central data collection, analysis, and trending component for the 1-to-N intelligent sensor array is called MedSPAN. From the network analogy you would consider MedSPAN to be the interface to McCOI.

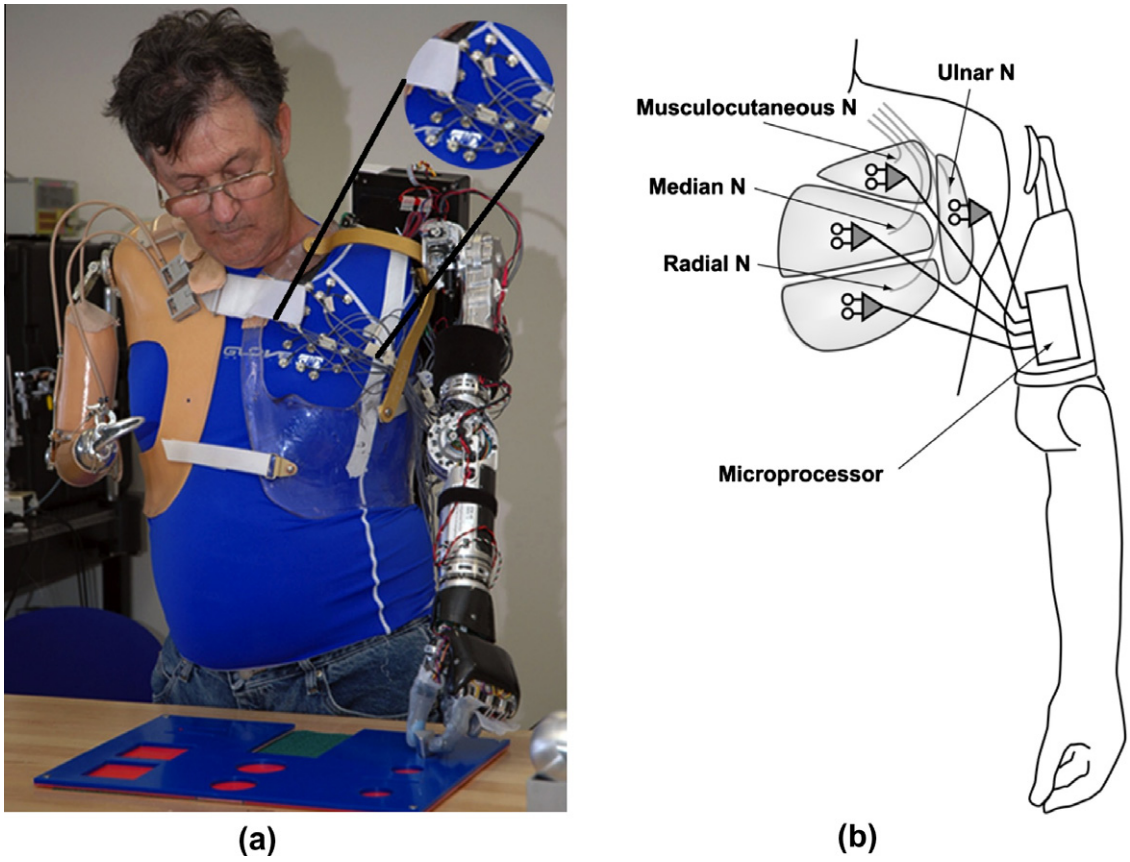

Fig. 4. Research Institute of Chicago's "Bionic Man": (a) Jesse Sullivan controls a robotic-enhanced prosthesis through targeted muscle reinnervation [22] (modified to highlight wired surface electrodes), (b) RIC system schematic of peripheral nerves to pectoralis major in shoulder disarticulation amputation [28] (N = nerve).

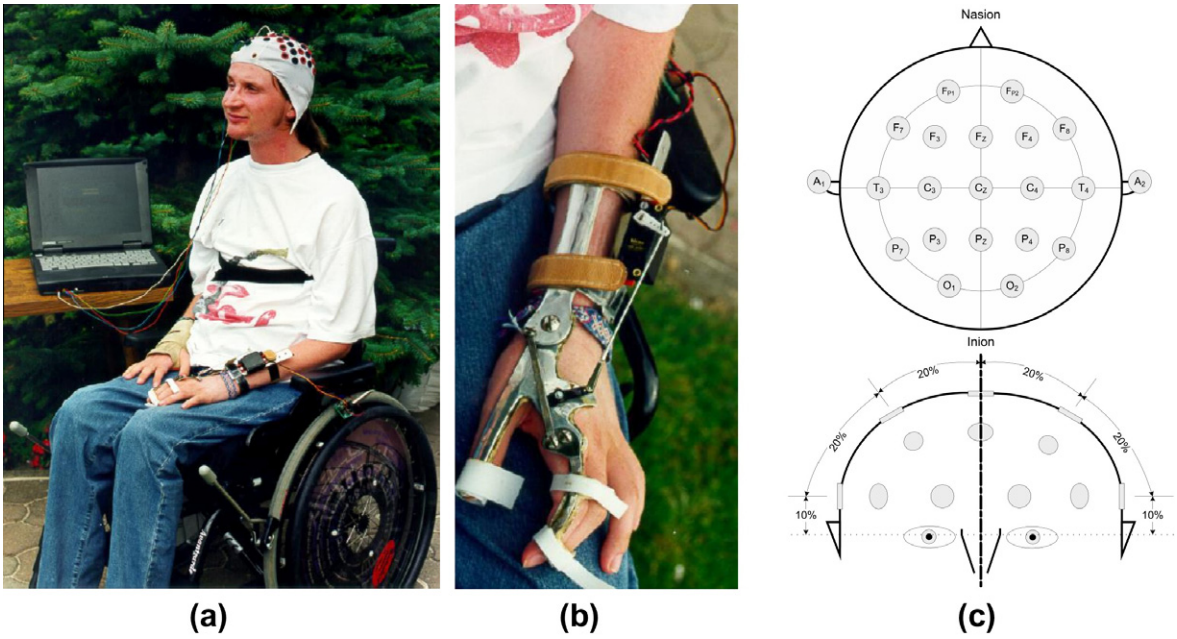

Fig. 5. Brain–Computer-Interface for tetraplegic control of a hand orthosis using surface electrodes in a standard 10–20 organization: (a) Tetraplegic subject employing BCI control [30], (b) the hand orthosis [30], and (c) the international 10–20 standard for EEG electrode placement [31].

The design of rehabilitative and assistive sensors for communication and control of a subject attribute (e.g., moving a mouse pointer for spelling, or muscular contraction for grasping) are similar to the type we would use in a medical monitoring or care application; however, these sensors would be more task focused and typically localized. Fig. 4a shows the application of surface

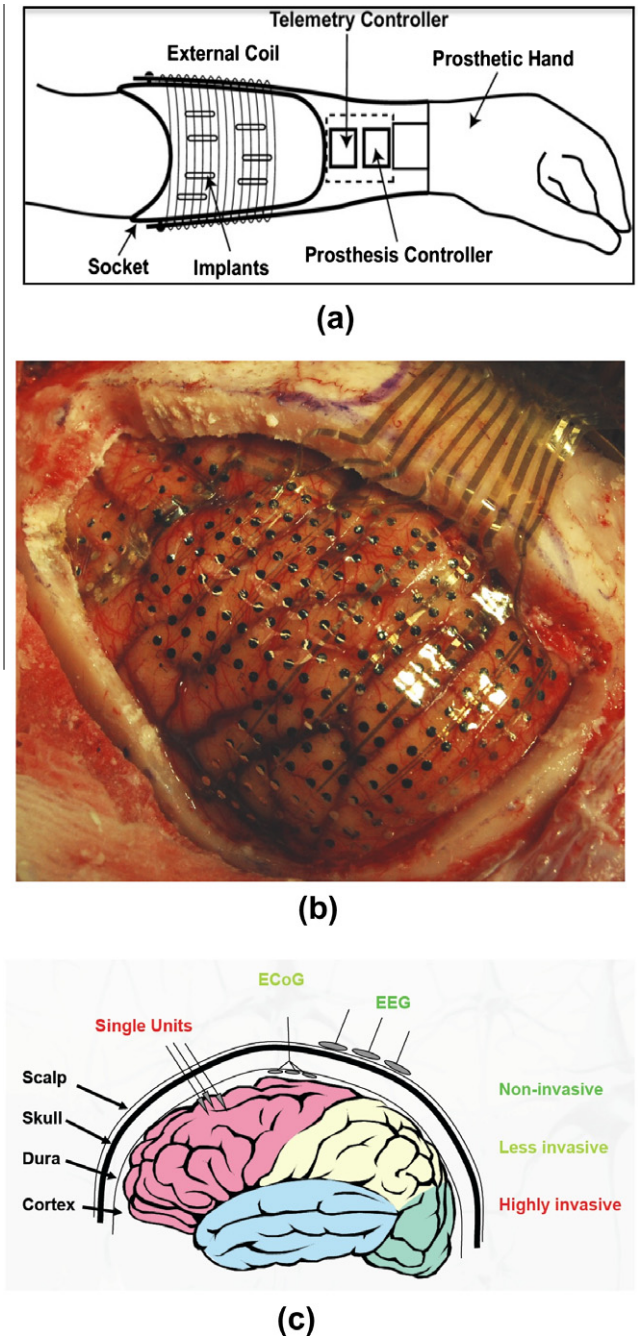

Fig. 6. (a) Implanted telemetry and control sensors for a prosthetic hand [32], (b) The Electrocorticographic (ECoG) electrode array overlaid directly on the human brain [33], and (c) levels of sensor/electrode invasiveness related to BCI [34].

electrodes used in myoelectric pattern recognition for control of an enhanced robotic prosthesis. Fig. 4b provides a conceptual schematic for how the system is realized. Note the number of surface electrodes required, the placement of each, and the physical wires connecting from the electrode to the embedded system controller. Fig. 5a and b show an alternate application of surface electrodes for the implementation of a brain–computer-interface that permits the subject, a tetraplegic, to control an orthosis for gripping. While the electrode location is standardized as shown in Fig. 5c using the international 10–20 system and typically BCI use less than the complete montage, the electrode application is a non-trivial task.

While clearly the wearable electrodes and sensors are least invasive, their efficient positioning and physical application is a topic that is generally not well considered for practical purposes.

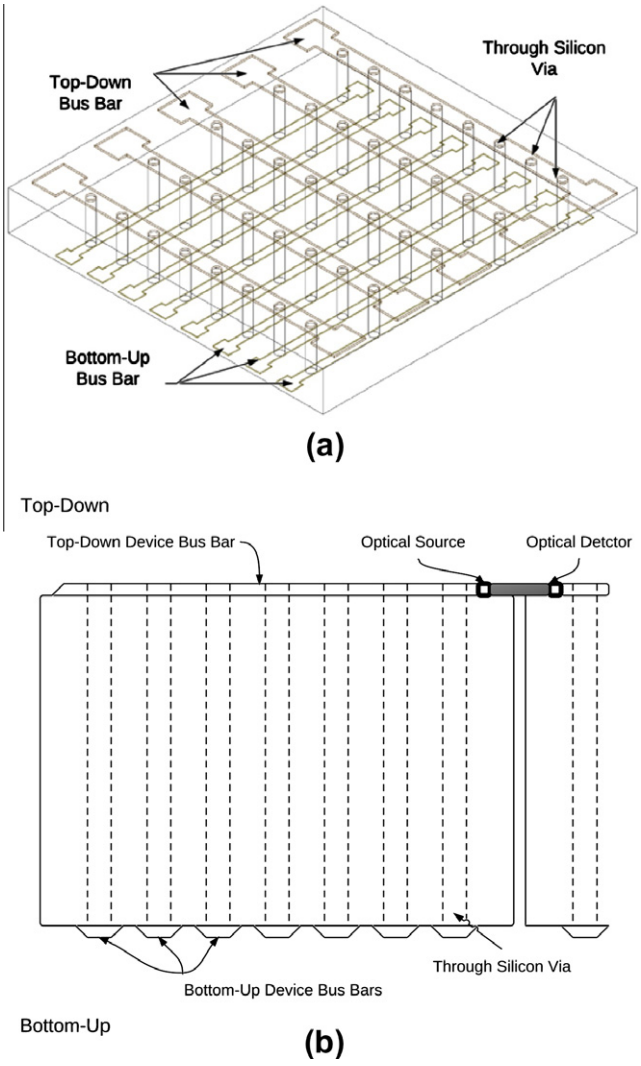

Fig. 7. (a) Through Silicon Via's (TSV) for top-down meets with bottom-up through bus-bar structure, and (b) Bus-bar unit shown in parallel with optical interconnect.

2.2.2. Implantable intelligent sensors

Implantable, intelligent sensors will require basic transducers, telemetry, and biocompatibility. Implantation has a range of invasiveness and generally is accepted by subjects that require or choose to it.

In comparison with the wearable surface system shown in Figs. 4 and 5, the benefits of an intelligent and biocompatible implant are very clear. An implanted sensor, as illustrated in Fig. 6a, would simplify the set up of an enhanced prosthetic for the subject. Consider the specialized support required to set up the electrodes for the prosthesis from Fig. 4.

The electrode array shown in Fig. 6b is a flexible grid that is laid directly on the subject's brain; this is ECoG, which directly measures the electrical signals from the cerebral cortex. This extreme form implantation is less invasive than the micro-electrode arrays that are inserted into the brain for measurement of single unit neurons and has shown promising results for highly functional BCI systems [35]. Fig. 6c illustrates the levels of invasiveness of BCI. While the results from ECoG are highly promising for BCI, the candidates are typically suffering from severe seizures and the procedure's primary focus is on localization and detection of the seizure events. A highly functional ECoG BCI that would offer a more reliable system than the BCI presented in Fig. 5 and it would facilitate a subject's independence in using the device; however, beyond the issues of

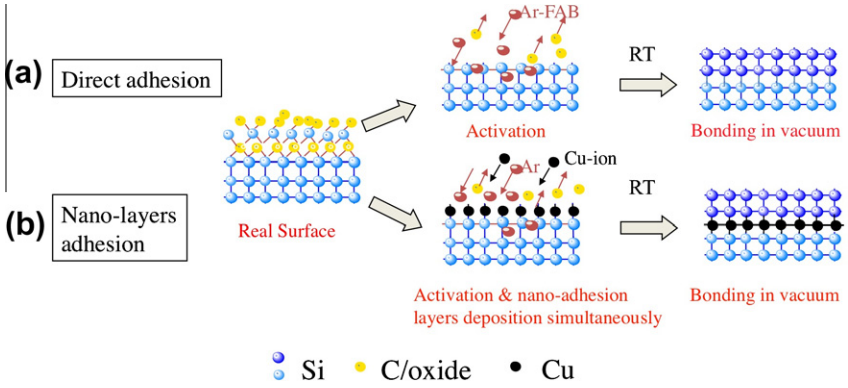

Fig. 8. Schematic diagram of two categories of surface-activation-based nanobonding technologies (a) direct adhesion and (b) nanolayers adhesion between the mated surfaces [16].

biocompatibility and long-term stability there is the obvious hurdle of getting the electrical signals from inside the subject out to the control system (as Fig. 6b shows, this is still done through direct wire). To mitigate some of the problems with wires exiting the biological system, micro-ECoG proposes focused electrode array that is fitted through a small hole in the skull and dura [36,37].

Given the nature of implantation and the biological system, the sensors must be flexible and biologically compatible or inert. For the sensor to conform to the biological structure, the appropriate material(s) must provide flexible lamination. As an example, liquid crystal polymer (LCP) bonded to gold would be suitable material for electrode/sensor development [38].

3. Top-down meets bottom-up

The top-down meets bottom-up challenge is further demonstrated when the emerging biomedical applications are considered because the bottom-up nano-scale devices must interface with top-down system [39]. To overcome this interface, we propose a bus-bar approach where bottom-up nano-scale devices can be interconnected to top-down systems by semiconductors NWs vertical "fusing" using Through Silicon Via (TSV). Fig. 7a illustrates the unit bus interconnection architecture. The bus-bar units may be used in parallel for multiple nano-scale devices, similar to the conceptual structure from Fig. 1. The connection between bus-bar units may be performed by directly, however the authors propose an optical source and detector, as shown in Fig. 7b, for electrical isolation between nano-scale devices. This optical source-detector and waveguide subsystem may be implemented with Gallium arsenide (GaAs)/Gallium phosphide (GaP) as described in Section 4.4. Note that GaAs is not a biocompatible material. This issue can be addressed by depositing biocompatible adsorption layers, for example a few tens of nanometers thick polymerized mercaptopropyl trimethoxysilane (MPT) thiol on GaAs [40]. For the bonding, it is desirable if the junction materials used would exhibit little to no effects (for example current density changes) under varying biomedical application temperatures (ambient or self-heating). The Copper/Gallium Arsenide (Cu/GaAs) [41] or Silicon/Gallium Arsenide (Si/GaAs) [42] bonding (as described in Section 4.3) methods may provide suitable solutions.

As new nano-scale bottom-up devices emerge and top-down methods evolve, there will be demand for bonding of new and potentially dissimilar materials. For longevity and biocompatibility the bonding method should produce very strong connections, have low toxicity (preferably chemical free), and provide direct adhesion. For the presented challenges of implanted sensors requiring external connections, it would certainly be advantageous to also have a biocompatible bonding method that meets these requirements, but also performs the bonding in air, without high external pressure, and at room temperature for system implementation in-situ.

4. Surface activated nanointegration at low temperature

Nanointegration has been demonstrated in diverse combinations of metals, semiconductors and insulators based on the surface activated nanobonding at room temperature. Surface activated nanobonding refers to the joining of dissimilar materials at nanometer scale through surface activation, which can be applied not only to the bulk materials, but also to the nanostructures/nanowires. Smooth surfaces with high surface flatness, low surface roughness and low thickness allow for the nanobonding after cleaning the surfaces. These parameters ensure intimate contact between the wafers to be bonded. The surfaces are cleaned by using argon (Ar) fast atom beam (Ar-FAB) or Ar low energy ion source. The etching rate of surfaces is typically as low as ~0.05 nm/s, which keeps the smoothness of the surfaces. Nanobonding can be classified into four categories. Fig. 8 is the schematic diagram showing two categories of nanobonding used in this review [16]. In the earlier approach, the mating surfaces are cleaned with an argon fast atom beam (Ar-FAB), and direct adhesion occurs when they are contacted in ultra-high vacuum (UHV) (Fig. 8a). In the second approach, the surface cleaning and nano-adhesion layer deposition are simultaneously done using an Ar ion source followed by contact in low vacuum (Fig. 8b) [16]. Generally, while the nanobonding accomplishes in a UHV pressure, it can be done also in air [16]. This depends on the reactivity of the surfaces in the bonding atmosphere. For example, while the activated copper surface oxidizes in air, the activated glass surface requires exposing to air before bonding. Therefore, the choice of surface activation and bonding medium is depended on the nature of surface in the bonding media. Compared with other existing direct bonding methods, the advantages of the surface activated nanobonding [16] are:

(1) bonding dissimilar materials in wide areas with high bond strength;
(2) no requirement of applying external pressure, adhesive, heat, or chemicals;
(3) sub-micrometer alignment accuracy;
(4) biologically compatible (i.e., non-toxic) interface;
(5) preserves delicate components and biological specimens; and
(6) mechanical, electrical, and optical connections on the same surface.

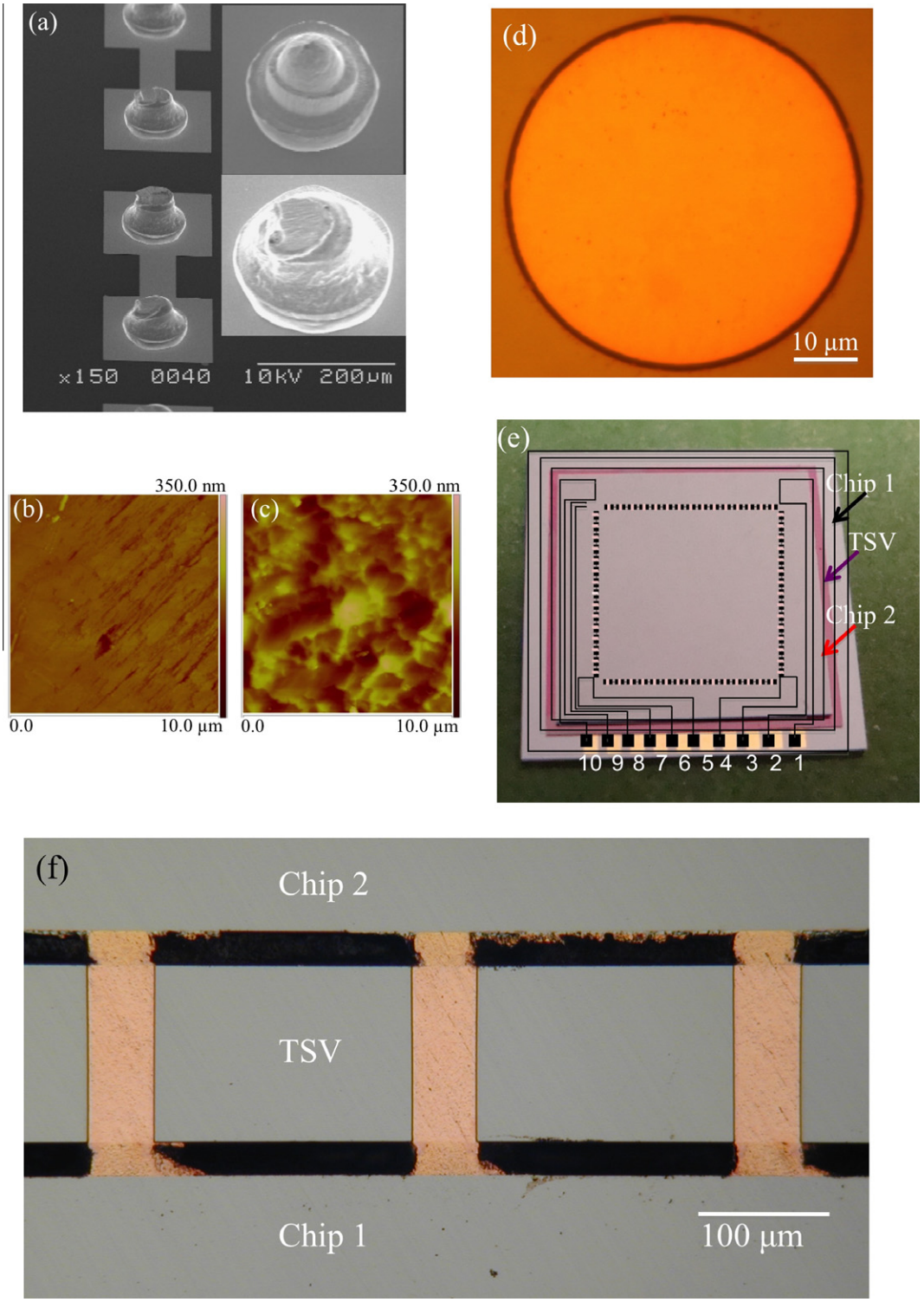

Fig. 9. (a) Scanning electron microscope images of the flattened Au-stud bumps with inset magnified images before and after flattening; AFM images of Au-stud bump surface over $10 \times 10\ \mu m^2$ of (b) deformed and (c) non-deformed areas; (d) optical image of Cu-TSV, (e) three-dimensional picture with schematic diagram of locations of electrodes and wirings, (f) cross-sectional optical image of Au-SB/Cu-TSV [43].

In Section 4, we discuss some of our recent research results of copper, gold, silicon, gallium arsenide, gallium phosphide and liquid crystal polymer (LCP) nanobonding for nanostructures and NWs integration for biomedical diagnostics and biochemical analysis. We describe results from nanobonding using the first approach (direct adhesion in UHV) for rigid substrates (i.e., silicon) at room temperature. Room temperature behavior of the bonding strength, electrical behavior and morphology of the interface along with thermal reliability was investigated.

In the second approach, we describe results from the nanobonding of flexible substrates (i.e., LCP) in low vacuum [16] that was heated 240 °C. Peel strength, electrical behavior and morphology of the interface along with frequency-conduction loss were investigated.

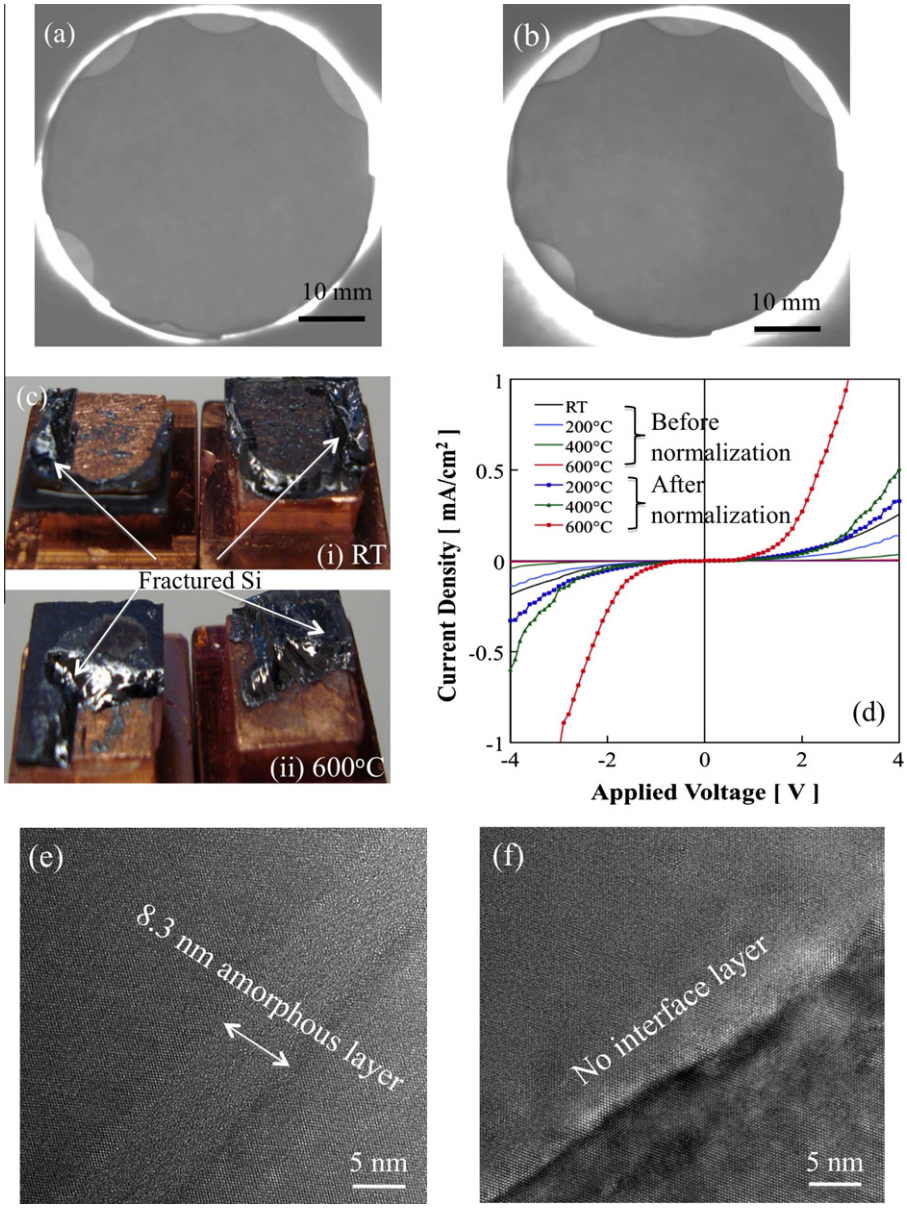

Fig. 10. Infrared (IR) transmission images (a) before annealing, (b) after annealing at 600 °C, (c) fractures images (i) before annealing and (ii) after annealing at 600 °C, (d) *I–V* characteristics of the *p*-Si/*p*-Si interface before and after annealing up to 600 °C, and HRTEM images of the interface (e) before and (f) after annealing at 600 °C [52].

4.1. Cu- through silicon vias (Cu-TSV)/Gold-stud bumps (Au-SBs)

Currently Cu- through silicon vias (Cu-TSV)/gold-stud bumps (Au-SBs) have been attracted for high-density interconnection in the miniaturization of biosensing and bioimaging systems [16,43,44]. A two-step process was used for the fabrication of Cu-TSV. First, using shallow and deep reactive ion etching, vias were fabricated in silicon followed by an insulation layer of silicon dioxide barrier. Second, for filling the vias, Cu was used in an electroplating technique [43–46]. Unfortunately, the shape of the top surface of stud bumps hinders intimate contact over wide area between Cu-TSVs and Au-SBs. To flatten the top surface of the stud bumps, an external compressive pressure of about 40 MPa was applied over each bump (external force 0.16 N/bump) on this surface [44,47]. This process improved the surface roughness and contact area that required for the nanobonding.

The surface roughness of the deformed area was 9.6 nm (Fig. 9b), which is significantly improved compared with that of non-deformed area (36.1 nm, Fig. 9c). The base and height of the Au-SBs were 50 and 37 μm, respectively. Through AFM investigations of TSV surface over $10 \times 10\ \mu m^2$ of area, the surface roughness was measured to be 6 nm. The Cu-TSVs and Au-SBs nanobonding was accomplished in UHV after surface activation using a 1.5 keV Ar-FAB with 48 mA for 300 s at room temperature [43,44]. Since this surface roughness of deformed Au-SBs and Cu-TSVs does not fully meet the requirement of nanobonding in UHV [44], a 20 N external force was applied for bonding at room temperature. A number of Cu-TSVs (120) were vertically sandwiched between two chips with Au-SBs, as shown in Fig. 9e.

After bonding, no considerable misalignment is observed in the cross-sectional view of the bonded Au stud bumps and Cu-TSV, as shown in Fig. 9f. In addition, the bonding strength of Au-SB and Cu-TSV through tensile pulling test was approximately as high as 110 MPa [43].

The electrical resistance of the interface, which includes two interfaces between Au-SB and Cu-TSV and the height of one Cu-TSV, was as low as 0.5 Ω [43,16]. A mechanical caulking technique has been reported to bond Au-SBs with TSVs to achieve

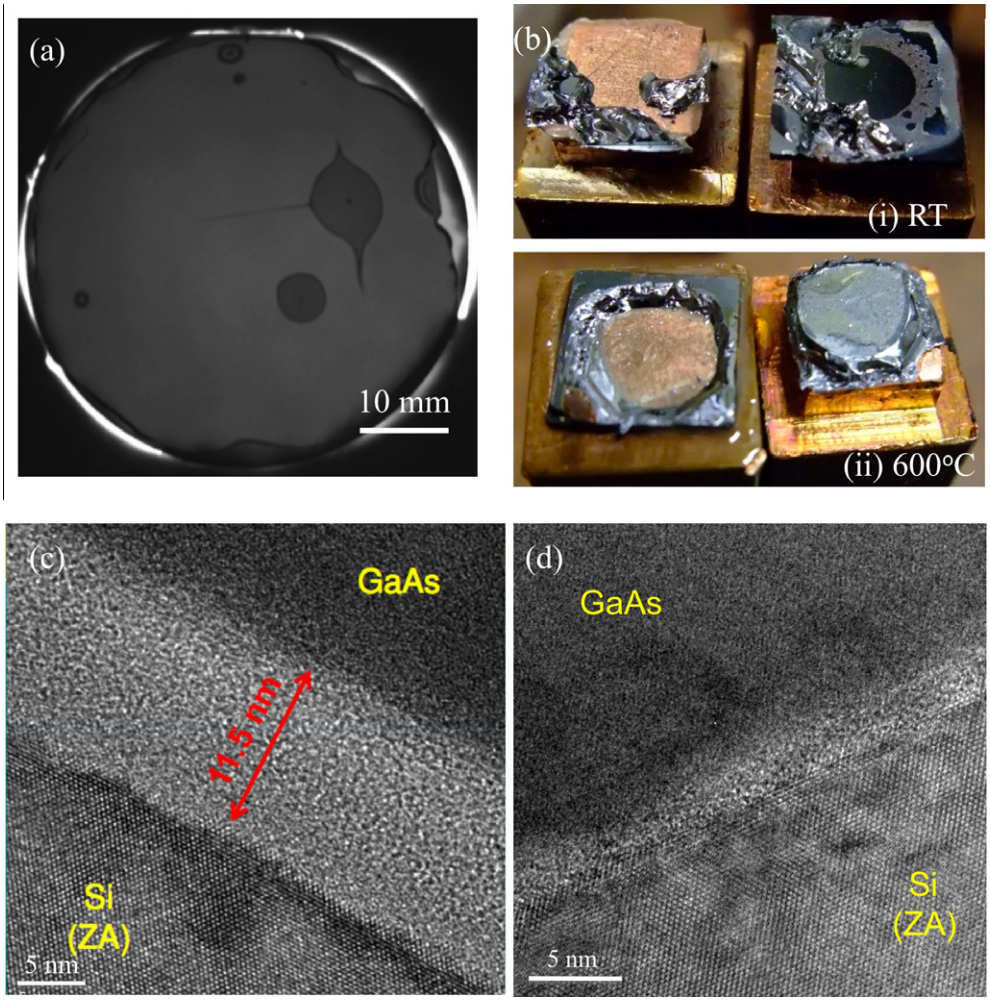

Fig. 11. (a) Infrared transmission image, (b) fracture images of Si/GaAs (i) before and (ii) after annealing at 600 °C, and HRTEM images (c) before and (d) after annealing at 600 °C. The specimens were bonded by using the nanobonding technology in UHV at room temperature [42].

three-dimensional (3D) assembly by applying compressive pressure to squeeze the former into the latter [47]. The compressive pressure is about 150 MPa, which is about 3.5 times higher than that of the pressure used in this work [43]. Therefore, the bonding between Au-SBs and Cu-TSVs at room temperature with low bonding pressure provides the feasibility of 3D-system integration with high-density interconnections for many applications such as biosensing and bioimaging systems [48–50].

4.2. Silicon/silicon (Si)

The capability of chemical-free strong bonding of Si wafers in nanobonding technologies has received remarkable attention for creating nanostructures and NWs based micro- and nano-scale devices such as nanorobots for monitoring of arterial disease [51]. Nanometer scale bonding provides the integration of miniaturized electronics, sensors, wireless power supply and data transmission, and packaging for such systems.

As received mirror polished Si wafers were bonded after activating surfaces using a 1.5 keV FAB with an amperage of 48 mA for 300 s and bonded in UHV at room temperature [52]. Fig. 10a shows the infrared (IR) transmission images of the interfaces of Si/Si bonded using the nanobonding technology in UHV at room temperature [52]. A void-free bonded interface was achieved in Si/Si. The comparison of the IR images of the Si/Si interfaces before annealing (Fig. 10a) and after annealing at 600 °C (Fig. 10b) indicates that there are no thermally induced voids at the interfaces [52]. The specimens were annealed for 1 h at every 200 °C.

The white and broken areas at the edges of the Si/Si bonded wafers are due to the blade test. The blade test was performed in order to measure the bonding strength of the wafers. The insertion of the blade at the bonded interface failed due to the high bonding strength of the Si/Si substrates. In order to investigate the bonding strength, the bonded wafers were diced into 10 mm × 10 mm squares and glued with copper jigs. High bonding strength with bulk fractures was observed. Fig. 10c shows the fracture images of Si/Si interfaces after tensile pulling test for the bonded specimen without annealing and after annealing at 600 °C [52]. Bulk fractured Si was remained on both sides of copper jigs. No interfacial delamination was observed after the tensile pulling test. The bonding strength of Si/Si was higher than 18 MPa as failure does not happen across the Si–Si interface. The high bonding strength is attributed to the covalent bonding between the atoms of the cleaned and smooth mated surfaces [52]. After annealing, the bonding strength was almost remained constant at different annealing temperatures.

The electrical transport behavior of the nanobonded interface can be evaluated by measuring the electrical characteristics of the bonded wafers. Fig. 10d shows the *I–V* behavior of *p*-Si/*p*-Si bonded wafers. The resistivity of the Si was 0.01–0.02 Ω cm. The electrode for Si was made by deposition of Au with 3 mm diameter before bonding for the ohmic contacts. Typical *I–V* curve of the *p–p* junction was observed.

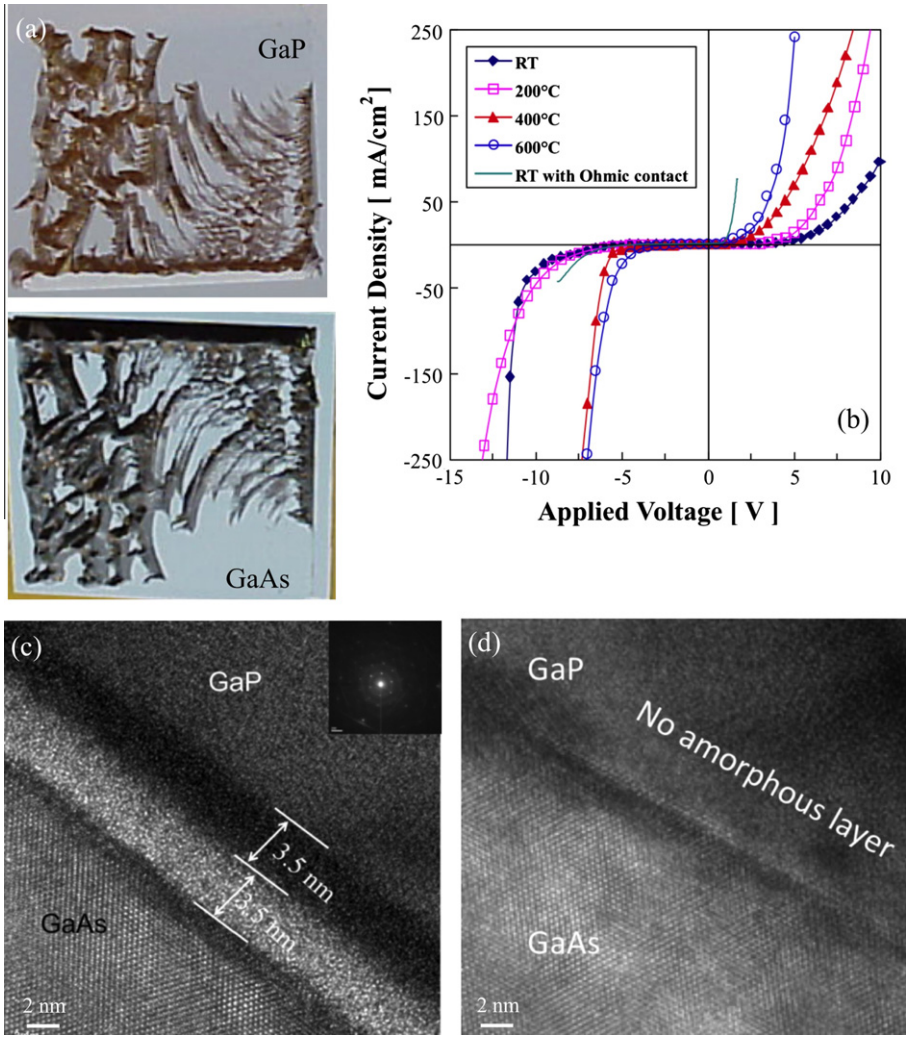

Fig. 12. Characteristics behavior of *p*-GaP/*n*-GaAs bonded interface. (a) Fracture images, (b) *I–V* characteristics with and without ohmic contacts, and HRTEM images (c) before and (d) after annealing at 600 °C [53].

Fig. 10e shows the HRTEM images of the interfaces of Si/Si bonded wafers [52] without heating. The interface was free from voids or fractures, but an interfacial amorphous layer with nanometer thickness was observed. An 8.3 nm thick amorphous layer was present at the bonded interface. It is well known that the interfacial amorphous layer is formed due to the surface damage during activation using Ar ion source [53,54]. After annealing at 600 °C, the amorphous layer was diminished, as shown in Fig. 10f. Finally, the annealing effect on the bonding strength and current conduction of the interfaces was correlated with that of the interfacial nanostructure.

4.3. Silicon/gallium arsenide (GaAs)

Heterogeneous semiconductor wafer bonding such as Si/GaAs can provide photonic integration on electronic platform [55]. This can be realized by using nanobonding technology in UHV at room temperature. For Si/GaAs bonding, the surface activation times for Si and GaAs were 300 s. Fig. 11a and b show the IR images and the fracture images of *p*-Si/*n*-GaAs bonded interface, respectively [42,56]. A number of voids due to the presence of particles on the activated surfaces were observed at the interfaces of Si/GaAs (Fig. 11a). Bulk fractured GaAs remained on Si after the tensile pulling test (Fig. 11b). The bonding strength of Si/GaAs was 14.4 MPa, while it was 18 MPa for Si/Si. In general, the bonding strength depends on the weaker wafer of the bonded pairs. Therefore, the relatively lower bonding strength of Si/GaAs than that of Si/Si can be due to the weaker strength of bulk of GaAs. After annealing, the bonding strength was almost remained constant at different annealing temperatures.

Fig. 11c and d show the HRTEM images of the interface of bonded Si/GaAs wafers before annealing and after annealing at 600 °C, respectively [42]. While the thickness of the interfacial amorphous layer was 11.5 nm, it was diminished at 600 °C. This is identical to that of Si/Si interface annealed at 600 °C. The thermal treatment improved the interfacial behavior as well as increased the current density at the interface.

4.4. Gallium arsenide (GaAs)/Gallium phosphide (GaP)

Interfacial behavior of mirror polished chip sizes of *n*-GaAs (100) and *p*-GaP (100) 15° off orientation with dimensions of $(10 \times 10 \times 0.35)$ and $(20 \times 20 \times 0.25)$ mm^3, respectively, was investigated [53]. The specimens were separately activated using 1.5 keV of Ar-FAB ions with a dose rate of 2.38×10^{14} i/cm^{2}s in a pressure of $<10^{-6}$ Pa for 180 s. The wafers were bonded in the bonding chamber under an external force of 60 kg f for 60 s. The bonding strength of the interface was 9.8 MPa at room temperature. Bulk fractured GaP was remained on the GaAs after the tensile pulling test (Fig. 12a).

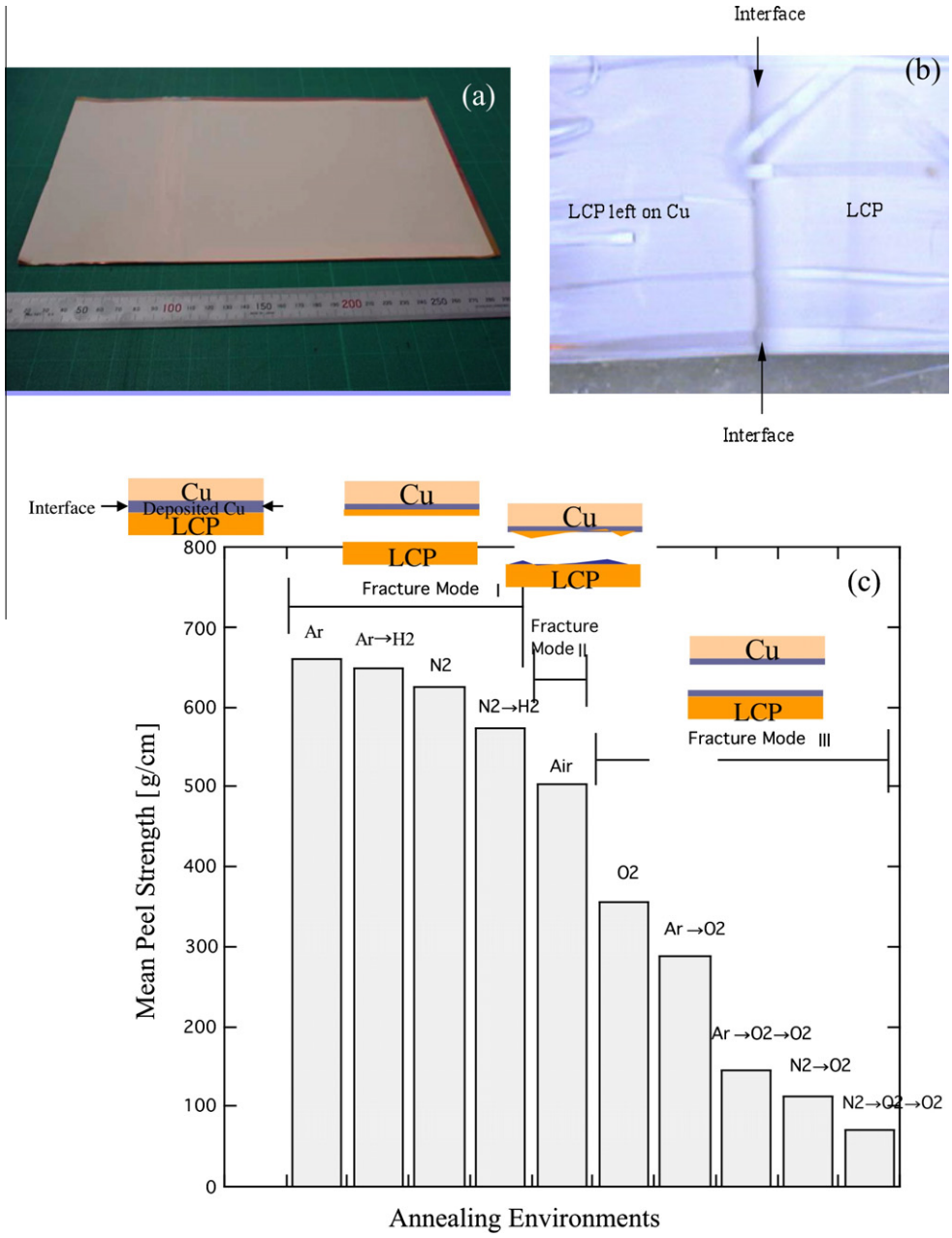

Fig. 13. (a) Optical image of Cu/LCP after heating in Ar gas; (b) optical image of partially peeled Cu and LCP surfaces with the interface; and (c) peel strength of Cu/LCP heating in N_2, Ar, air, and O_2 gases [58–60].

The current density of the *p*–*n* junction was increased with the increase of the applied voltage in the specimens with Ohmic and nonohmic electrodes, as shown in Fig. 12b [53]. High ideality factor of *p*-GaP/*n*-GaAs junction was observed. The high ideality factor was attributed to the prolonged activation as well as a high carrier concentration. The barrier heights for the nonohmic electrodes were decreased as the annealing temperature increased. The barrier height was decreased with increasing the annealing temperature. This temperature dependent decrease in barrier height indicates a decrease of interface defect states, which act as recombination centers for traps. The electrical current density was increased with the increase of the annealing temperature. Annealing temperature dependent breakdown voltages were observed. The breakdown voltages were reduced with the increase of the annealing temperature in the forward and reverse biases.

Fig. 12c and d show the nanostructure of the bonded GaP/GaAs interfaces before annealing and after annealing at 600 °C, respectively [53]. Before annealing, two amorphous layers with identical thicknesses of 3.5 nm were observed at the interface without annealing. The amorphous layers were generated due to surface damage caused by Ar atom implantation during activation. However, the amorphous layers prohibit fracturing due to CTE mismatch while heating. The thickness of the amorphous layers, adjacent to the GaP side, was reduced from 3.5 nm to 3.0 nm upon annealing at 200 °C. When the annealing temperatures were increased to 400 °C and 600 °C, the amorphous layers diminished. After annealing, the interfacial electrical current conduction was improved and the amorphous layers were diminished. The amorphous layers, adjacent to the GaP across the interface, attribute to the Ga-rich layer because of the depletion of phosphorus [53]. Thus, the reduced amorphous layer thickness upon annealing improved the *I*–*V* characteristics.

High bonding strength irrespective of annealing temperatures, improved current density even at room temperature and nanometer

scale bonding results of Si/Si, Si/GaAs and GaP/GaAs are needed for the integration of nanostructures. Therefore, the findings can be applied in spontaneous integration of nanostructures and NWs on the wafer scale required for the micro- and nano-scale systems.

4.5. Cu/liquid crystal polymer (LCP) nanobonding in low vacuum

Recently, flexible lamination of Cu and liquid crystal polymer (LCP) has been demanded for microelectronics, MEMS and implantable biomedical microsystems due to low conduction loss, low-water uptake and biocompatibility [39,57]. However, the challenges for the lamination are low adhesion, low mechanical stability, and high electrical resistance at the interface [58,59]. Cu has been bonded with LCP using the second approach of the nanobonding. In this case, the activated LCP surface with nanoadhesion layers requires heating after contacting with the activated Cu. The heating is required because of high-surface roughness of polymer surface after activation (and even before activation), and the deposition of nanoadhesion layers. In this approach, the Cu and LCP surfaces were sputter cleaned with Ar-RF plasma etching in a background vacuum pressure of 3×10^{-3} Pa to remove the contamination and native oxide layers on the surface. After surface cleaning, Cu was deposited on the LCP, and the two were bonded directly at room temperature [60]. Subsequently, the Cu/LCP specimens were heated in an Ar gas below the glass transition temperature of LCP (i.e., at 240 °C for 1 h). This process resulted in higher interface adhesion than that in the conventional heat-laminated process.

Fig. 13 shows (a) the optical image of Cu/LCP after heating in Ar gas; (b) the optical image of partially peeled Cu and LCP surfaces with the interface; and (c) the peel strength of Cu/LCP heating in N_2, Ar, air, and O_2 gases [58]. After bonding, the Cu/LCP was curled due to residual stress (not shown) at the interface. Heating relieved the residual stress and flattened the laminate (Fig. 13a). The optical image after the peeling test showed bulk fracture of LCP for the specimens heated in an Ar environment [58], indicating higher interfacial adhesion strength than that of bulk LCP material. The peel strength of Cu/LCP was dependent on the type of gas used in the heating. The peel strength of specimens heated in Ar and N_2 was considerably higher than that of specimens heated in air and O_2. The peel strength of the sequentially heated specimens in O_2 gas that already heated in Ar and N_2 gases was significantly reduced. A comparative investigation on C1s, O1s, and Cu2p3/2 spectra of the plasma activated and delaminated surfaces has been accomplished using an x-ray photoelectron spectroscope. A carbon-rich LCP surface with a reduced amount of oxygen after sputter cleaning with RF plasma was observed, which was reacted with the deposited Cu. Therefore, the adhesion mechanism of Cu/LCP is the bonding of Cu adhesion sites (cleaned) to plasma-induced dangling sites of LCP surface (Cu deposited), and thermal reconstruction of Cu deposited layers when heating in Ar and N_2 gases. This is in contrast to mechanical interlocking across the interface utilized for adhesion improvement in the conventional lamination of polymer to metal. While heating in air or O_2, the oxidized Cu layers was produced across the interface due to the reaction of diffused oxygen in LCP with deposited Cu layers. This resulted in weak bonding in air or O_2.

The advantages of enhanced adhesion in the nanobonding lamination of Cu/LCP can be realized through pattering of fine-pitches and measuring the frequency dependent conduction losses [59,60]. Fig. 14 shows (a) the SEM image of the etching patterns of Cu on LCP; (b) the frequency-dependent conduction loss of LCP/Cu interface compared with that of conventional heat laminate; and (c) the frequency dependence of the conductivity of LCP/Cu interface [59,60]. Fine-pitch Cu patterns with line and space 50 μm was built on LCP. The fine-pitch patterns were intact while folded and

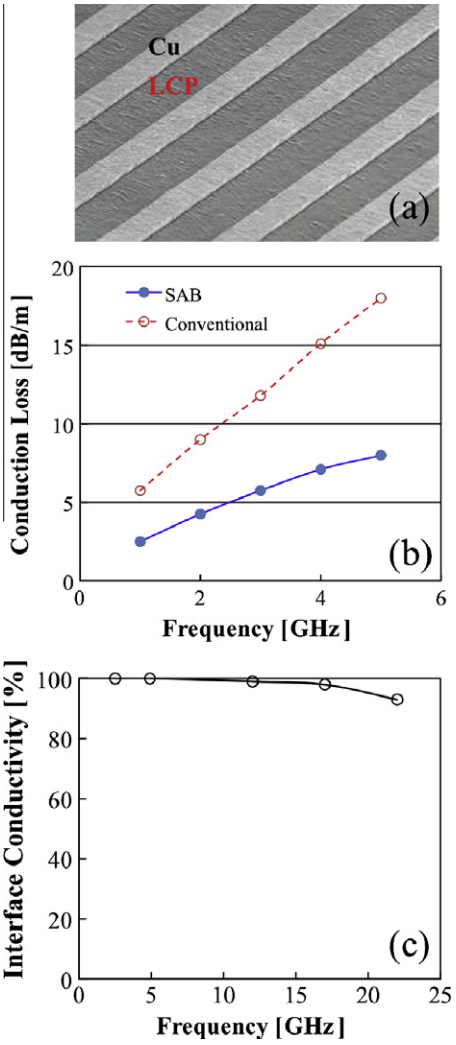

Fig. 14. (a) SEM image of the etching patterns of Cu on LCP; (b) frequency-dependent conduction loss of LCP/Cu interface compared with that of conventional heat laminate; and (c) frequency dependence of the conductivity of LCP/Cu interface (adapted from Refs. [59,60]).

bended the laminate. The measured conduction loss in both the nanobonding (SAB) and conventional laminates increases with the increase of frequency. A three-fold lower loss for the nanobonding laminate was observed compared with the conventional heat laminate. The smooth interface attributes to the low loss of the nanobonding laminate. Therefore, the lower contact area of Cu/LCP across the interface compared to the conventional heat laminate was responsible for the lower loss in the nanobonding laminate. Further, the influence of high frequency on the interfacial conductivity of Cu/LCP was examined [59,60]. Here, a 10 μm thick Cu–Zr alloy was bonded with a 50 μm thick LCP with the 19-nm sputtered Cu–Ni alloy. The interfacial conductivity was decreased to some extent with the increase of the frequency, but remained above 90% even at 20 GHz. This indicates the potential of nanobonded laminates for high frequency processing within an intelligent sensor.

5. Perspectives and conclusions

The design integration of top-down systems and bottom-up devices is simplified using the authors presented bus-bar unit. This method of simplifying nanointegration lends itself to the inherent design approach from both system and device approaches. In order

for the field of nanointegration to contribute to the emerging biomedical applications, the characteristics of such systems must be better understood. Nano-scale development for applications of intelligent sensors for remote patient monitoring and rehabilitation systems require advances in nanointegration for complete realization. The requirements for nanointegration of such biomedical systems are best suited to the surface activated nanobonding method because it permits biocompatible, high performance, and miniaturized systems with strong junction and interface bond, low toxicity, and favorable electrical properties.

Acknowledgments

This research was supported by a Discovery Grant (No. 327947) and an Engage Grant (No. 412206) from the Natural Science and Engineering Research Council of Canada and an infrastructure Grant (No. 12128) from the Canada Foundation for Innovation (CFI). The authors would like to thank Prof. M. Jamal Deen of McMaster University for the support and assistance in establishing nano-bonding and interconnection research at the Micro- and Nano-Systems Laboratory, Prof. Tadatomo Suga of The University of Tokyo, who is the pioneer of the surface activated bonding, for the for the contribution in this work, Prof. M.J. Kim of the University of Texas at Dallas for the contribution of nanointerfacial characterization, F. Zhang of McMaster University for her assistance in the bonding and characterization, and the Canada Center for Electron Microscopy (CCEM) at McMaster University for the assistance in the HRTEM experiments.

References

[1] Jokerst JV, Jacobson JW, Bhagwandin BD, Floriano PN, Christodoulides N, McDevitt JT. Programmable nano-bio-chip sensors: analytical meets clinical. Anal Chem 2010;82(5):1571–9.
[2] Rolfe P. Medical and biological measurement with micro- and nano-sensors. Optoelectron Instrument Proc 2010;46(4):324–8.
[3] Preethichandra DMG, Ekanayake EMIM. Nano-biosensor development for biomedical and environmental measurements. New Develop Appl Sens Technol 2011:279–92.
[4] Goldberg M, Langer R, Jia X. Nanostructured materials for applications in drug delivery and tissue engineering. J Biomater Sci Polym Ed 2007;18(3):241–68.
[5] Liong M, Lu J, Kovochich M, Xia T, Ruehm SG, Nel AE, et al. Multifunctional inorganic nanoparticles for imaging, targeting, and drug delivery. ACS Nano 2008;2(5):889–96.
[6] Wang H, Sun M, Ding K, Hill MT, Ning CZ. A top-down approach to fabrication of high quality vertical heterostructure nanowire arrays. Nano Lett 2011;11(4):1646–50.
[7] Schlipf M, Bathurst S, Kippenbrock K, Kim SG, Lanza G. A structured approach to integrate MEMS and precision engineering methods. CIRP J Manufac Sci Technol 2011;3(3):236–47.
[8] Maury P, Peter M, Mahalingam V, Reinhoudt DN, Huskens J. Patterned self-assembly monolayers on silicon oxide prepared by nanoimprint lithography and their applications in nanofabrication. Adv Func Mater 2005;15(3):451–7.
[9] Li Q, Koo S-M, Richter CA, Edelstein MD, Bonevich JE, Kopanski JJ, et al. Precise alignment of single nanowires and fabrication of nanoelectromechanical switch and other test structures. IEEE Trans Nanotechnol 2007;6(2):256–63.
[10] Cao L, Chen S, Wei D, Liu Y, Fu L, Yu G, et al. Fabrication and characterization of molecular scale field-effect transistors. J Mater Chem 2010;20(12):2305–9.
[11] Komanduri R, Chen J, Malshe A, Doumanidis C, Rajurkar K. NSF-EC workshop on nanomanufacturing and processing: a summary report. Proc SPIE 2002;4936:446–54.
[12] Yang N, Uetsuka H, Williams OA, Osawa E, Tokuda N, Nebel CE. Vertically aligned diamond nanowires: fabrication, characterization, and application for DNA sensing. Phys Status Solidi A 2009;206(9):2048–56.
[13] Guo LJ. Nanoimprint technology and its applications. Proc SPIE 2005;5734:53–64.
[14] Thompson SE, Parthasarathy S. Moore's law: the future of Si microelectronics. Mater Today 2006;9(6):20–5.
[15] Lee BH, Oh J, Tseng HH, Jammy R, Huff H. Gate stack technology for nanoscale devices. Mater Today 2006;9(6):32–40.
[16] Howlader MMR, Selvaganapathy PR, Deen MJ, Suga T. Nanobonding technology toward electronic, fluidic and photonic systems integration. IEEE J Select Topics Quant Elect 2011;17(3):689–703.
[17] Crnogorac F, Wong S, Pease RFW. Semiconductor crystal islands for three-dimensional integration. J Vac Sci Technol B 2010;28(6). C6P53–C6P58.
[18] Kiefer AM, Paskiewicz DM, Clausen AM, Buchwald WR, Soref RA, Lagally MG. Si/Ge junctions formed by nanomembrane bonding. ACS Nano 2011;5(2):1179–89.
[19] Tan CS. Thermal characteristic of Cu–Cu bonding layer in 3-D integrated circuits stack. Microelectron Eng 2010;87(4):682–5.
[20] Karle TJ, Halioua Y, Raineri F, Monnier P, Braive R, Le Gratiet L, et al. Heterogeneous integration and precise alignment of InP-based photonic crystal lasers to complementary metal–oxide semiconductor fabricated silicon-on-insulator wire waveguides. J Appl Phys 2010;107(6):063103–11.
[21] Vesborg PCK, Olsen JL, Henriksen TR, Chorkendorff I, Hansen O. Note: anodic bonding with cooling of heat-sensitive areas. Rev Scient Instrum 2010;81:016111–3.
[22] Schultz AE, Kuiken TA. Neural interfaces for control of upper limb prostheses: The state of the art and future possibilities. 2011;3(1):55–67.
[23] Stein RB, Mushahwar V. Reanimating limbs after injury or disease. Trends Neurosci 2005;28(10):518–24.
[24] Di Pino G, Guglielmelli E, Rossini PM. Neuroplasticity in amputees: main implications on bidirectional interfacing of cybernetic hand prostheses. J Prog Neurobiol 2009;88(2):114–26.
[25] Kane MJ, Breen PP, Quondamatteo F, ÓLaighin G. BION microstimulators: a case study in the engineering of an electronic implantable medical device. J Med Eng Phys 2011;33(1):7–16.
[26] Brunner P, Bianchi L, Guger C, Cincotti F, Schalk G. Current trends in hardware and software for brain–computer interfaces (BCIs). J Neural Eng 2011;8(2):1–7.
[27] McFarland DJ, Wolpaw JR. Brain–computer interfaces for communication and control. J Commun ACM 2011;54(5):60–6.
[28] Stubblefield KA, Miller LA, Lipschutz RD, Kuiken TA. Occupational therapy protocol for amputees with targeted muscle reinnervation. J Rehab Res Dev 2009;46(4):481–8.
[29] Brunner P, Ritaccio AL, Emrich JF, Bischof H, Schalk G. Rapid communication with a P300 matrix speller using electrocorticographic signals (ECoG). Front Neurosci 2011;5(0):9.
[30] Pfurtscheller G, Guger C, Müller G, Krausz G, Neuper C. Brain oscillations control hand orthosis in a tetraplegic. Neurosci Lett 2000;292:211–4.
[31] Richey ET, Namon R. EEG instrumentation and technology. Charles C. Thomas; 1976.
[32] Weir RFF, Troyk PR, DeMichele GA, Kerns DA, Schorsch JF, Maas H. Implantable myoelectric sensors (IMESs) for intramuscular electromyogram recording. IEEE Trans Biomed Eng 2009;56:159–71.
[33] Oostenveld R. ECoG brain dynamics in high-resolution recordings. In: 5th BCI2000 workshop & international workshop on advances in electrocorticography. NY, USA: Bolton Landing; October 1–3, 2009.
[34] Leuthardt EC. Utilization of BCI for potential treatment of hemispheric stroke. in: 5th BCI2000 workshop & international workshop on advances in electrocorticography. NY, USA: Bolton Landing; October 1–3, 2009.
[35] Kubánek J, Miller KJ, Ojemann JG, Wolpaw JR, Schalk G. Decoding flexion of individual fingers using electrocorticographic signals in humans. J Neural Eng 2009;6(6):066001–14.
[36] Schalk G, Miller KJ, Anderson NR, Wilson JA, Smyth MD, Ojemann JG, et al. Two-dimensional movement control using electrocorticographic signals in humans. J Neural Eng 2008;5:75–84.
[37] Ledochowitsch P, Félus RJ, Gibboni RR, Miyakawa, Bao S, Maharbiz MM. Fabrication and testing of a large area, high density, parylene MEMS μECoG array. In: IEEE 24th International Conference on Micro Electro Mechanical Systems (MEMS), 2011; 2011. p. 1031–4.
[38] Li C, Sauser FE, Azizkhan RG, Ahn CH, Papautsky I. Polymer flip-chip bonding of pressure sensors on a flexible Kapton film for neonatal catheters. J Micromech Microeng 2005;15:1729–35.
[39] Lu W, Lieber CM. Nanoelectronics from the bottom up. Nat Mater 2007;6:841–9.
[40] Kirchner C, George M, Stein B, Parak WJ, Gaub HE, Seitz M. Corrosion protection and long-term chemical functionalization of gallium arsenide in an aqueous environment. Adv Func Mater 2002;12(4):266–76.
[41] Leau WK, Chu JP, Lin CH. Interfacial reaction and electrical characteristics of Cu(RuTaNx) on GaAs: annealing effects. Appl Surf Sci 2011;257(16):7286–90.
[42] Yu T, Howlader MMR, Zhang F, Bakr M. Nanobonding for multi-junction solar cells at room temperature. ECS Trans 2011;35(2):3–10.
[43] Howlader MMR, Zhang F, Deen MJ, Suga T, Yamauchi A. Surface activated bonding of copper through silicon vias and gold stud bumps at room temperature. J Vac Sci Technol A 2010;29:021007–17.
[44] Howlader MMR, Yamauchi A, Suga T. Surface activation based nano-bonding and interconnection at room temperature. J Micromech Microeng 2011;21(2):025009–10.
[45] Wang X, Zeng W, Eisenbraun E. Sub-0.25 micron silicon via etching for 3D Interconnects. J Micromech Microeng 2007;17:804–11.
[46] Spiesshoefer S, Patel J, Lam T, Cai L, Polamreddy S, Figueroa RF, et al. Copper electroplating to fill blind vias for three-dimensional integration. J Vac Sci Technol A 2006;24(4):1277–82.
[47] Tanaka N, Yoshimura Y, Kawashita M, Uematsu T, Miyazaki C, Toma N, et al. Through-silicon via interconnection for 3D integration using room-temperature bonding. IEEE Trans Adv Packag 2009;32(4):746–53.
[48] Wang TD, Dam JV. Optical biopsy: a new frontier in endoscopic detection and diagnosis. Clin Gastroenterol Hepatol 2004;2(9):744–53.
[49] Kfouri M, Marinov O, Quevedo P, Faramarzpour N, Shirani S, Liu LW-C, et al. Towards a miniaturized wireless fluorescence-based diagnostic imaging system. IEEE J Select Topics Quant Elect 2008;14(10):226–34.

[50] El-Desouki M, Deen MJ, Fang Q, Liu L, Tse F, Armstrong D. CMOS image sensors for high speed applications. Sensors 2009;9(1):430–44.
[51] Cavalcanti A, Rosen L, Shirinzadeh B, Rosenfeld M. Nanorobot for treatment of patients with artery occlusion. Proc Virtual Concept; 2006.
[52] Howlader MMR, Zhang F. Void-free strong bonding of surface activated silicon wafers from room temperature to annealing at 600 °C. Thin Solid Films 2010;519:804–8.
[53] Howlader MMR, Suga T, Zhang F, Lee TH, Kim MJ. Interfacial behavior of surface activated *p*-GaP/*n*-GaAs bonded wafers at room temperature. Electrochem Solid State Lett 2010;13(3):H61–5.
[54] Takagi H, Maeda R, Hosoda N, Suga T. Transmission electron microscope observations of Si/Si interface bonded at room temperature by Ar beam surface activation. Jpn J Appl Phys 1999;38(3A):1589–94.
[55] Fang AW, Park H, Jones R, Cohen O, Paniccia MJ, Bowers JE. Heterogeneous integration of silicon and AlGaInAs for a silicon evanescent laser. Proc SPIE 2006;6133. 61330W1–61330W8.
[56] Howlader MMR, Watanabe T, Suga T. Investigation of the bonding strength and interface current of *p*-Si/*n*-GaAs wafers bonded by surface activated bonding at room temperature. J Vac Sci Technol B 2001;19(6):2114–8.
[57] Stieglitz T, Beutel H, Meyer J. Microflex—a new assembling technique for interconnects. J Intell Mater Sys Struc 2000;11(6):417–25.
[58] Howlader MMR, Iwashita M, Nanbu K, Saijo K, Suga T. Enhanced Cu/LCP adhesion by pre-sputter cleaning prior to Cu deposition. IEEE Trans Adv Packag 2005;28(3):495–502.
[59] Nanbu K, Ozawa S, Yoshida K, Saijo K, Suga T. Low temperature bonded Cu/LCP materials for FPCs and their characteristics. IEEE Trans Compon Packag Technol 2005;28(4):760–4.
[60] Howlader MMR, Suga T, Takahashi A, Saijo K, Ozawa S, Nanbu K. Surface activated bonding of LCP/Cu for electronic packaging. J Mater Sci 2005;40(12):3177–84.